

This document is confidential and is proprietary to the American Chemical Society and its authors. Do not copy or disclose without written permission. If you have received this item in error, notify the sender and delete all copies.

Revealing the nature of defects in α -Ag₂WO₄ by positron annihilation lifetime spectroscopy: A joint experimental and theoretical study

Journal:	<i>Crystal Growth & Design</i>
Manuscript ID	Draft
Manuscript Type:	Article
Date Submitted by the Author:	n/a
Complete List of Authors:	Assis, Marcelo; Universidade Federal de Sao Carlos, Ponce, Miguel; INTEMA Gouveia, Amanda; Universidade Federal de Sao Carlos, CDMF Souza, Daniele; UFSCar da Costa, João Paulo; Universidade de Sao Paulo Escola de Engenharia de Sao Carlos, Electrical and Computer Engineering Teodoro, Vinícius; Universidade Federal de Sao Carlos, Gobato, Yara; UFSCar Andrés, Juan; Universitat Jaume I, Química Física i Analítica Macchi, Carlos; Universidad Nacional del Centro de la Provincia de Buenos Aires Somoza, Alberto; Instituto de Física de Materiales Tandil - IFIMAT, Universidad Nacional del Centro de la Provincia de Buenos Aires, Física Longo, Elson; Universidade Federal de Sao Carlos, CDMF-UFSCar

SCHOLARONE™
Manuscripts

1
2
3 **Revealing the nature of defects in α -Ag₂WO₄ by positron annihilation**
4
5
6 **lifetime spectroscopy: A joint experimental and theoretical study**
7
8
9

10 Marcelo Assis^{1*}, Miguel Adolfo Ponce², Amanda Fernandes Gouveia^{1,3}, Daniele
11 Souza⁴, João Paulo de Campos da Costa¹, Vinicius Teodoro¹, Yara Galvão Gobato⁴,
12 Juan Andrés⁵, Carlos Macchi⁶, Alberto Somoza⁶, Elson Longo¹
13
14
15

16
17
18 ¹CDMF, LIEC, Chemistry Department - Federal University of São Carlos - (UFSCar),
19 P.O. Box 676, 13565-905 São Carlos, SP, Brazil.

20
21 ²Institute of Materials Science and Technology (INTEMA), Mar del Plata, Argentina.

22
23 ³Institute of Chemistry, State University of Campinas, Unicamp, 13083-970, Campinas,
24 SP, Brazil.

25
26 ⁴Physics Department - Federal University of São Carlos - (UFSCar), P.O. Box 676,
27 13565-905 São Carlos, SP, Brazil.

28
29 ⁵Department of Physical and Analytical Chemistry, University Jaume I (UJI), Castelló
30 12071, Spain.

31
32 ⁶CIFICEN (UNCPBA-CICPBA-CONICET) and Instituto de Física de Materiales
33 Tandil (UNCPBA), Pinto 399, B7000GHG Tandil, Argentina.
34
35
36
37
38
39
40
41
42
43
44
45
46
47
48
49
50
51
52
53
54
55
56
57
58
59
60

ABSTRACT

Electron-matter coupling is a fascinating way to tune and modify the properties of materials. In this work, we present a study on the formation and nature of vacancy-like defects in α -Ag₂WO₄ samples synthesized in an aqueous or ethanol medium and subsequently submitted to electron beam irradiation at different exposure times. To understand the effects on the geometrical and electronic nature of the generated defects, the data obtained by positron annihilation lifetime spectroscopy were interpreted with the aid of first-principle calculations at the density functional theory level. To complement these results, X-ray diffraction, Raman spectroscopy, photoluminescence emissions and field emission gun scanning electron microscopy techniques were also used. Based on the positron binding energy and the calculated and experimental positron lifetimes, the defect structure of the non-irradiated and irradiated samples was revealed. As a general feature, it was found that the defect structure is more complex for samples synthesized in ethanol than in water. In particular, the results show that all samples contain defects involving Ag vacancies and that the concentration of this type of defect increases with the irradiation time.

Keywords: α -Ag₂WO₄, point defects, positron annihilation lifetime spectroscopy, DFT calculations.

1. INTRODUCTION

The chemical and physical properties of semiconductors are largely determined by the population of defects, which have attracted continuous attention owing to their significant influence on such properties. Due to the similarity to enzymes, the domain where defects appear in the semiconductor structures can be considered active sites in which reactivity takes place and functionality occurs. At concentrations where defects do not interact with each other, they can be represented by individual electronic states isolated within the band of the host material, whose orbital and spin degrees of freedom can be controlled through the use of electromagnetic fields. However, there are still many challenges to be addressed, and further studies are necessary to unveil the nature and effects of the defects in semiconductors¹⁻³.

In the field of solid materials, the ideal crystal formed by the periodic replication of unit cells does not exist. In reality, crystals are exposed to lattice vibrations, contain defects and have surface and bulk vacancies, impurities and non-stoichiometric compositions⁴⁻⁷. For scientists, the management of the presence of defects, which can be associated with a structural and electronic disorder, may enable the creation of new materials with unique, impossible physical properties for well-ordered crystal structures⁸⁻¹¹. To understand the nature of the defects and their formation and removal mechanisms in semiconductors constitutes a very challenging topic in materials science¹¹⁻¹³.

Positron annihilation lifetime spectroscopy (PALS) is a well-recognized non-destructive nuclear technique to obtain specific information regarding structural and electronic aspects of open volume defects in solids¹⁴. The advantages of the use of PALS to study defects lie in the fact that positrons are prone to be localized and annihilated in sites with greater electronic density (i.e. more negative) than the average electronic density of the crystal lattice, allowing positron annihilation processes to take place in these sites, which act as positron traps with an associated specific open volume. In particular, PALS

1
2
3 has demonstrated to be a powerful tool to investigate the presence of vacancy-like
4 defects in semiconductors^{15,16}. This technique has also been successfully used to obtain
5 information on the defect structure of monocrystalline and polycrystalline
6 semiconductor metal oxides¹⁷⁻²⁴. In fact, vacancies in neutral or negative charge states
7 act as efficient positron traps due to the reduced repulsion of positive ions, while
8 positive vacancies do not trap positrons. On the other hand, it is well documented that
9 multiple vacancies or vacancy clusters are even more effective positron traps than single
10 vacancies. In this case, the charge-state dependence is the same as that described for
11 vacancies. Every time an open volume exists in a defect complex, it appears for the
12 positron as a vacancy-like defect, that is, if a negative ion is bound to a vacancy this
13 defect appears as an effective positron trap. It must be said that the effectiveness of this
14 trap depends on the total charge of the vacancy complex. Under this frame, a neutral
15 pair consisting of a negative ion and a positive vacancy also acts as an effective positron
16 trap with the positron localized inside the vacancy²⁵.

17
18
19
20
21
22
23
24
25
26
27
28
29
30
31
32
33
34
35
36
37
38
39
40
41
42
43
44
45
46
47
48
49
50
51
52
53
54
55
56
57
58
59
60
There has been a growing interest in silver tungstate (α -Ag₂WO₄) due to its unique
properties with a wide range of applications in the field of environmental remediation,
photocatalysis, etc.²⁶. α -Ag₂WO₄ has a crystal lattice composed of distorted [WO₆] and
[AgO_y] (y= 2, 4, 6, and 7) clusters acting as lattice building blocks, displaying a
complex 3D structure. This distinctive structure is responsible for a wide range of
technological applications. From an electronic point of view, the top of the valence band
(VB) consists of unique hybridized Ag 4*d* and O 2*p* orbitals, which can leave the top
position of the VB and narrow down the band gap. The bottom of the conduction band
(CB) comprised of delocalized *s* and/or *p* orbitals presents significant dispersity, which
means that it possesses high migration efficiency of photogenerated electrons.²⁷⁻²⁹

1
2
3 With the substantial developments of electron microscopes and their beam sources, the
4 use of transmission electron microscopes is no more limited to materials
5 characterization. Recently, different research studies have focused on the effect of
6 electron beam irradiation (EBI) on the generation of defects since more and more
7 related applications have been unveiled.^{30–38} Under EBI, energy is transferred from
8 energetic electrons to both electrons and atomic nuclei in the target materials. In this
9 context, our research group has demonstrated that EBI on materials could be employed
10 for advanced fabrication, modification, and functionalization of α -Ag₂WO₄. Its
11 enhanced performance is strongly dependent on the large anisotropy produced by the
12 complex structure of the α -Ag₂WO₄ oxide, which leads to the generation of defects.
13
14
15
16
17
18
19
20
21
22
23
24
25
26
27
28
29
30
31
32
33
34
35
36
37
38
39
40
41
42
43
44
45
46
47
48
49
50
51
52
53
54
55
56
57
58
59
60

27,29,39-55 Therefore, it is necessary a deep knowledge of the structure, nature and concentration of defects at nano- and sub-nanometric scales resulting from the α -Ag₂WO₄ material modification due to EBI for a rational optimization of their properties and the search for new applications. To the best of our knowledge, a systematic investigation on the type of defects and their nature in α -Ag₂WO₄ provoked by EBI has not been conducted yet.

The main goals of the present work are two-fold: (i) to gain a deeper understanding of the formation process and nature of atomic defects in α -Ag₂WO₄ under EBI as a function of the solvent used for the synthesis of the samples, that is, water (WT) and ethanol (AL). The experimental information on these defects was obtained using PALS as well as X-ray diffraction (XRD) with Rietveld refinements, Raman spectroscopy, photoluminescence (PL) emissions, field emission gun scanning electron microscopy (FEG-SEM); and (ii) to understand the fine effects of the geometrical and electronic nature of the generated defects. For this purpose, first-principle calculations at the

1
2
3 density functional theory (DFT) level were performed to complement and rationalize
4 the experimental PALS results.
5
6

7 This paper contains additional three sections. In the Experimental Section below we
8 report the sample synthesis and characterization as well as the computational methods
9 and model systems employed. In section three we present and discuss the obtained
10 results. Finally, the conclusions are summarized in the final section.
11
12
13
14
15
16
17
18

19 **2. EXPERIMENTAL SECTION**

20
21 **2.1. Synthesis.** The synthesis of α -Ag₂WO₄ samples was performed by the co-
22 precipitation (CP) method in aqueous (WT) and ethanol (AL) media at 70°C. The
23 details and reagents used followed the description made by Foggi et al.⁴⁵. α -Ag₂WO₄
24 semiconductor powder was cold-pressed at a pressure of ~ 500 MPa into circular pellets
25 with 5 mm in diameter and ~ 1 mm in thickness.
26
27
28
29
30
31
32

33 **2.2. EBI.** To obtain the materials irradiated with electrons, the pellet samples of α -
34 Ag₂WO₄ were placed in a FE-SEM microscope, model Supra 35-VP (Carl Zeiss,
35 Germany), with an acceleration voltage of 30 kV for 3 (WT3, AL3), 6 (WT6, AL6) and
36 9 (WT9, AL9) min.
37
38
39
40
41

42 **2.3. Characterization.** The α -Ag₂WO₄ samples were structurally characterized by XRD
43 using a D/Max-2500PC diffractometer (Rigaku, Japan) with CuK α radiation ($\lambda = 1.5406$
44 Å) in the 2θ range between 10°-110°, at a scan speed of 1°min⁻¹ in the Rietveld routine.
45 The Rietveld refinements were performed in the General Structure Analysis System
46 (GSAS) program. Micro-Raman spectra were recorded using the iHR550 spectrometer
47 (Horiba Jobin-Yvon, Japan) equipped with a charge-coupled device (CCD) detector and
48 an argon-ion laser (Melles Griot, USA) operating at 514.5 nm with a maximum power
49 of 200 mW, and a fiber microscope. The morphologies, textures and sizes of the
50
51
52
53
54
55
56
57
58
59
60

1
2
3 samples obtained were observed with a FEG-SEM microscope (Supra 35-VP, Carl
4 Zeiss, Germany) operated at 10 kV. PL measurements were performed at room
5 temperature (RT) using a 500M Spex spectrometer coupled to a GaAs PMT. A Kimmon
6 He-Cd laser (325 nm line) with laser power up to 40 mW was used as the excitation
7 source.
8
9

10
11
12
13
14 **2.4. PALS.** PALS spectra were obtained using a fast-fast spectrometer with a time
15 resolution of 251 ps in a collinear geometry. A 10 μCi -sealed source of $^{22}\text{NaCl}$
16 deposited onto two thin Kapton foils (7.5- μm thick) sandwiched between two identical
17 samples was used as a positron source. The spectra were acquired at RT, and typical
18 1.5-2 $\times 10^6$ counts per spectrum were collected. The lifetime values reported in this work
19 for each sample are at least an average of ten measurements in the same experimental
20 conditions. After subtracting the background and the source contribution, the PALS
21 spectra were analyzed using the LT10 program ⁵⁶.
22
23
24
25
26
27
28
29
30
31

32
33 **2.5. Computational methods and model systems.** First-principles calculations
34 at the DFT level were carried out using the Viena *ab initio* simulation package
35 (VASP) version 5.4.4 ^{57,58}. The semi-local Perdew-Burke-Ernzerhof ⁵⁹ exchange
36 and the correlation energy functional within the spin-polarized generalized
37 gradient approximation (GGA) formulation were employed. The Kohn-Sham
38 equations were solved using the projector augmented wave (PAW) method ⁶⁰,
39 employing the following projectors: Ag ($4d^{10}, 5s^1$), W ($5p^6, 5d^4, 6s^2$), and O
40 ($2s^2, 2p^4$), where the numbers in parentheses represent the valence states. In the
41 calculation, a Gaussian smearing of 0.01 eV was used, and the atoms were
42 allowed to relax until all forces were smaller than 0.01 eV/Å on every atom and
43 the equilibrium volume of crystals was obtained by the minimization of stress
44 tensor through a plane wave cut-off of 834 eV and another of 469 eV to optimize
45
46
47
48
49
50
51
52
53
54
55
56
57
58
59
60

1
2
3 the atomic force. For the Brillouin zone integration, a k -mesh of $1 \times 1 \times 2$ for stress
4 tensor and atomic force optimizations were employed.
5
6

7
8 To obtain the theoretical positron lifetimes (τ) for the bulk and vacancy states in the α -
9 Ag_2WO_4 structure, calculations were performed according to Macchi et al.⁶¹. The
10 positron parameters were calculated using DFT within the so-called standard scheme⁶².
11
12 The positron wave functions, the parameters τ and the positron binding energy (E_b)
13 were obtained through the Doppler program included in the MIKA package⁶³,
14 considering as an input parameter the electron density calculated by VASP.
15
16

17
18 The positron binding energy is defined as the difference between the ground energy E_0
19 of the delocalized positron and the energy of the positron trapped in the considered
20 defect (E_d):
21
22

$$E_b = E_0 - E_d \quad (\text{Eq. 1})$$

23
24 This energy indicates the energy gained for a positron trapped in a specific defect. A
25 positive sign for E_b indicates that the considered defect acts as a positron trapping
26 center.
27
28

29
30 To get positron parameters, it is necessary to calculate the electron-positron correlation
31 potential. To this end, the local density approximation (LDA) was considered by
32 employing the parameterization proposed by Boronski and Nieminen⁶⁴. Such
33 parameterization was corrected to take into account the incomplete positron screening
34⁶², in which the value of the high-frequency dielectric constant was measured as
35 follows: *ad-hoc* ($\epsilon_\infty = 17.6$).
36
37

38
39 To model the orthorhombic α - Ag_2WO_4 structure, we used the relaxed cell previously
40 described⁶⁵. A supercell of 672 atoms ($2 \times 2 \times 3$ repetitions of the relaxed cell) was used
41 to calculate the positron lifetimes in the different defect states, considering different
42 supercells containing: i) an oxygen monovacancy (V_O); ii) a tungsten monovacancy (V_W)
43
44
45
46
47
48
49
50
51
52
53
54
55
56
57
58
59
60

1
2
3); iii) a silver monovacancy (V_{Ag}); iv) a divacancy constituted by silver and oxygen (V_{Ag}
4 + V_O); v) a trivacancy formed by one silver vacancy and two oxygen vacancies (V_{Ag} +
5 + V_O); and finally, a hexavacancy containing two silver and four oxygen vacancies ($2V_{Ag}$
6 + $4V_O$). In the present work, different oxygen vacancies were modeled by removing an
7 O atom from the different clusters that are the building blocks of the α - Ag_2WO_4 crystal
8 structure ($[WO_6]$ and $[AgO_x]$ ($x = 2, 4, 6$ and 7) clusters). The V_W was created by
9 removing a W atom from the $[WO_6]$ cluster located near the center of the supercell. In
10 the case of four non-equivalent V_{Ag} belonging to the different $[AgO_x]$ clusters ($x = 2, 4,$
11 6 and 7), an Ag atom at each of the four possible $[AgO_x]$ clusters was removed.
12 Additionally, for each V_{Ag} different vacancies were modeled by removing one or two
13 oxygen atoms that are the nearest neighbors to each V_{Ag} in order to form a divacancy or
14 a trivacancy ($V_{Ag} + V_O$ and $V_{Ag} + 2V_O$, respectively). To form a hexavacancy, two
15 adjacent trivacancies ($V_{Ag} + 2V_O$) were considered.

16
17
18
19
20
21
22
23
24
25
26
27
28
29
30
31
32
33
34 As a first approach, a further relaxation of the defective structures was not taken into
35 account for all calculations. Besides, all defect states were considered in their neutral
36 states. It is worth mentioning that for different semiconductors the calculated positron
37 lifetimes for defects in the negative charge states are always slightly shorter (between
38 $\sim 2\%$ and $\sim 8\%$, depending on the considered negative charge state) than those
39 determined for the same semiconductor containing defects in its neutral states^{66,67}.

3. RESULTS AND DISCUSSION

40
41
42
43
44
45
46
47
48
49
50
51
52 **3.1. X-Ray Diffraction.** XRD analysis was performed in order to understand the
53 structural order/disorder of the materials at long range (periodicity and organization) in
54 relation to the solvent (WT and AL) used and its subsequent modification by EBI. **Fig.**
55
56
57
58
59 **SI-1** (see Supporting Information) shows the corresponding XRD patterns. According to
60

1
2
3 the analysis of the results, all samples correspond to α -Ag₂WO₄ with orthorhombic
4 structure and *Pn2n* space group, which is in accordance with the crystallographic record
5 No. 248969⁶⁸ in the *Inorganic Crystal Structure Database* (ICSD). All samples have
6 well-defined peaks, which are associated with a high degree of long-range order. No
7 additional peaks were observed, demonstrating that the pure α -Ag₂WO₄ phase was
8 obtained in both solvents and also after modification by EBI.
9

10 The lattice parameters (*a*, *b* and *c*) as well as the cell volume (*v*), full width at half
11 maximum (FWHM) and reliability parameters (*R*_{wp}, *R*_p, χ^2) was obtained by Rietveld
12 refinements and are shown in **Figure SI-2** and **Table SI-1**. The reliability parameters
13 obtained in the Rietveld refinement indicate that the results have a high degree of
14 quality. It was observed that for the samples synthesized in WT or AL and subjected to
15 EBI, there was an increase in the values of the lattice parameters and unit cell volume.
16 These changes can be directly related to the FWHM of the main α -Ag₂WO₄ diffraction
17 peak (231) at $2\theta = 32^\circ$. According to **Table SI-1**, the FWHM increases with the EBI
18 time, causing the appearance of a more disordered system.³⁹
19
20
21
22
23
24
25
26
27
28
29
30
31
32
33
34
35
36

37 **3.2. Micro-Raman Spectroscopy.** According to our group's theory, the orthorhombic
38 α -Ag₂WO₄ structure belongs to the C_{2v}^{10} symmetry group, which has 21 active Raman
39 modes from the decomposition point $\Gamma = (6A_{1g} + 5A_{2g} + 5B_{1g} + 5B_{2g})$. Although all 21
40 modes are active in Raman, in this case only 9 of them can be observed (see **Fig. SI-3**)
41 due to the overlapping of some modes as well as the high degree of disorder of the
42 systems at short range. Previous results⁴⁴ point out that the vibrational modes located at
43 106 and 317 cm⁻¹ are related to [AgO_x] clusters (*x* = 2, 4, 6, and 7), while the
44 vibrational modes located between 600 and 1000 cm⁻¹ refer to the O-W-O bending
45 angles and W-O stretching bonds of the [WO₆] clusters²⁸.
46
47
48
49
50
51
52
53
54
55
56
57
58
59
60

1
2
3 **3.3. Field Emission Gun Scanning Electron Microscopy.** The morphologies, particle
4 sizes and textures of all prepared pellet samples of α -Ag₂WO₄ (WT and AL) were
5 investigated by FE-SEM, and the results are presented in **Fig. SI-4**. It was observed that
6 both WT (**Fig. SI-4(A)**) and AL (**Fig. SI-4(B)**) samples have rod-like morphology with
7 hexagonal shape and (001), (010) and (101) exposed surfaces. From the analysis of the
8 results (see **Fig. SI-5**), the average length and width of the rods of the WT sample are
9 0.37 ± 0.13 and 0.13 ± 0.10 μm , respectively, while for the AL sample the
10 corresponding values are 0.66 ± 0.17 and 0.27 ± 0.13 μm .

11
12
13
14
15
16
17
18
19
20
21 **Fig. 1** shows the behavior of the WT (**Figs. 1(A) to 1(D)**) and AL (**Figs. 1(E) to 1(H)**)
22 pellets under EBI at voltage of 30 kV for 0, 3, 6 and 9 min. We noted that the exposure
23 to the electron beam generates the delocalized growth of some metallic Ag particles on
24 the surface of α -Ag₂WO₄. This phenomenon was reported in previous studies, and it is
25 due to the reduction of the Ag⁺ cation at both [AgO₂] and [AgO₄] clusters, thus
26 generating Ag metal nanoparticles on the semiconductor surface^{28,29,46,48,50,69,70}.

27
28
29
30
31
32
33
34
35
36
37
38 <**Figure 1**>

39
40 **Figure 1.** FE-SEM of WT samples irradiated for **(A)** 0, **(B)** 3, **(C)** 6 and **(D)** 9 min, and
41 AL samples irradiated for **(E)** 0, **(F)** 3, **(G)** 6 and **(H)** 9 min.

42
43
44
45
46
47 **3.4. Photoluminescence**

48
49 PL measurements provide important information about the structural defects in the
50 crystal lattice. **Fig. SI-6** exhibits the PL spectra of α -Ag₂WO₄ samples at room
51 temperature with laser excitation at 325 nm. The behavior of the PL spectra is
52 associated with multiphonon processes, where the relaxation of electron momentum
53 occurs by several paths with the participation of various energy intermediate states
54
55
56
57
58
59
60

1
2
3 within the forbidden band gap region ^{71–73}. The spectra arise from the octahedral [WO₆]
4 and [AgO_x] (x = 2, 4, 6 and 7) clusters, with maximum emission centered in the blue-
5 green region at 449 nm^{28,45,65,74}. The luminescence mechanism of these materials is
6 assigned to the charge transfer within the [WO₆] clusters, from the 2*p* orbital of O atom
7 and 4*d* orbital of Ag atom of the VB to the 5*d* orbital of the W atom of the CB.
8 Moreover, it is known that a modified crystal lattice, i.e. a lattice with increased
9 structural defect density, also favors the emission in the blue-green region, which is
10 more energetic.^{28,75} In particular, the PL emissions can be associated with the electronic
11 transitions from the ¹A₁ ground state to the ¹T₂ excited state corresponding to the
12 octahedral [WO₆] cluster ^{73,76}. In order to understand the PL behavior of all samples, the
13 PL spectra were deconvoluted to investigate the contributions of the individual
14 components using a Voigt function and considering the peak positions and their
15 respective areas, as seen in **Fig. SI-6**. For all samples, the spectra were decomposed into
16 two components centered at 450 and 490 nm, contributing to the blue and green colors
17 of the visible spectrum, respectively (see **Fig. 2**).

37
38
39
40 <Figure 2>

41
42 **Figure 2.** Percentages of PL deconvolution components for samples located at (A) 450
43 and (B) 490 nm as a function of EBI time.

44
45
46
47
48
49 After the deconvolution process, the contribution of the band centered at 450 nm
50 slightly decreases, while the band centered at 490 nm increases. This can be related to
51 structural defects (shallow defects) of the band located at shorter wavelengths and
52 vacancy defects (deep defects) of the band at longer wavelengths, revealing an increase
53 in the number of vacancies as a function of EBI exposure time. Besides that, it was
54
55
56
57
58
59
60

1
2
3 observed that the increased number of defects is more pronounced in the AL than the
4
5 WT synthesized samples.
6

7 **3.5. PALS Measurements**

8
9
10 From the spectra decomposition, several lifetime components could be obtained, being
11
12 each of them characterized by a lifetime τ_i and having an associated intensity I_i . The
13
14 state i can be delocalized in the crystal lattice (bulk state), or localized at different defect
15
16 sites in which positrons become trapped and annihilated. In this last case, the value of
17
18 the positron lifetime reflects the size of the open volume associated with the defect in
19
20 which positrons are annihilated. Increased lifetime values indicate that positrons
21
22 become trapped in bigger open volumes.
23
24

25
26 All PALS spectra obtained in the present work were satisfactorily fitted considering
27
28 three lifetime components. Initially, a free constraint fitting analysis showed the
29
30 presence of an almost constant long-lived lifetime, $\tau_3=1800\pm 100$ ps, usually assigned to
31
32 the ortho-Positronium (o-Ps) annihilation via the pick-off process. Then, a second
33
34 analysis was carried out fixing this component at 1800 ps. As a result, a small value of
35
36 intensity associated with τ_3 ($I_3 < 2\%$) was obtained, indicating that the powder
37
38 compression process used to fabricate the pellets was good enough to produce well-
39
40 compacted samples. It is worth mentioning that this long lifetime component related to
41
42 the small value of I_3 was not considered for further discussions. I_1 and I_2 were then
43
44 normalized to 100%.
45
46
47

48
49 On the other hand, α -Ag₂WO₄ microcrystals present a particle size higher than the
50
51 typical positron diffusion length, $L_+ \sim 100$ nm, in solids.¹⁴ In this scenario, it was
52
53 assumed that almost all positrons are annihilating in defects located inside the grains
54
55 (*i.e.* intragranular defects). Values of the positron lifetime parameters obtained from the
56
57
58
59
60

1
2
3 decomposition of the PALS spectra measured on samples synthesized in WT and AL
4 solvents are reported in **Tables 1** and **2**, respectively.
5
6
7
8
9

10 **Table 1.** Values of positron lifetimes and their associated intensities obtained from the
11 decomposition of PALS spectra for α -Ag₂WO₄ microcrystalline WT samples irradiated
12 and non-irradiated at different times.
13
14
15

16 <Table 1>
17
18
19
20

21 **Table 2.** Values of positron lifetimes and their associated intensities obtained from the
22 decomposition of PALS spectra for α -Ag₂WO₄ microcrystalline AL samples irradiated
23 and non-irradiated at different times.
24
25
26
27

28 <Table 2>
29
30
31
32

33 First-principles calculations are extremely useful for the interpretation and
34 rationalization of the experimental results of PALS measurements. The calculated
35 positron lifetimes and the corresponding binding energies of the supercell containing
36 different vacancy-like defects are presented in **Table 3**.
37
38
39
40
41
42
43

44 **Table 3.** Values of positron lifetimes, τ , and binding energy, E_b , for different positron
45 defect states in the α -Ag₂WO₄ structure.
46
47
48

49 <Table 3>
50
51
52
53

54 From the analysis of the calculated E_b values reported in **Table 3**, we can infer that
55 independently of the type of cluster from which one oxygen atom was extracted, V_O can
56 hardly trap positrons even in its neutral charge state. This behavior is due to the
57
58
59
60

1
2
3 delocalization of the positron wavefunction. This effect can be seen in **Fig. 3(A)**, where
4
5 it is possible to visualize a positron wavefunction isodensity plot calculated for V_O
6
7 created between two clusters (one $[\text{WO}_6]$ and one $[\text{AgO}_4]$). On the contrary, cation
8
9 vacancies such as V_W and V_{Ag} act as effective positron traps, which is in good agreement
10
11 with the results reported in the literature for semiconducting oxides.^{15,17,18} The cationic
12
13 vacancy V_W is not a deep positron trap since its binding energy is small when compared
14
15 to that calculated for V_{Ag} in different cluster structures, that is, ~ 0.1 eV *versus* ~ 0.6
16
17 eV. In **Table 3**, it can also be seen that the positron lifetime for $V_W = 178$ ps is barely
18
19 4% higher than that calculated for the $\alpha\text{-Ag}_2\text{WO}_4$ bulk of the supercell ($\tau_b = 172$ ps).
20
21 This behavior can be attributed to a weak localization of the positron wavefunction in
22
23 the defect, according to the isodensity plot in **Fig. 3(B)**. As observed, the positron
24
25 wavefunction is mostly localized in the interstitial space near the missing W atom. In
26
27 the case of the cationic vacancy V_{Ag} , remarkable changes in the calculated positron
28
29 parameters are not sensed, except for the V_{Ag} at the $[\text{AgO}_6]$ cluster. In particular, when
30
31 an Ag atom is extracted from an $[\text{AgO}_2]$ cluster, there is a strong increase in the positron
32
33 lifetime with respect to τ_b , resulting in a calculated positron lifetime approximately 33%
34
35 higher than τ_b and a positron binding energy of 0.6 eV. If V_{Ag} occurs at the $[\text{AgO}_7]$ or
36
37 $[\text{AgO}_4]$ cluster, the corresponding τ and E_b values are slightly smaller than those
38
39 obtained for the same vacancy created in an $[\text{AgO}_2]$ cluster. Conversely, for a V_{Ag}
40
41 created in an $[\text{AgO}_6]$ cluster, more significant changes in the positron parameters can be
42
43 obtained, which are reflected in a strong localization of the positron wavefunction
44
45 within the empty space left by the missing Ag atom. As an example, **Figs. 3(C)** and
46
47 **3(D)**, display positron wavefunction isodensity plots calculated for the monovacancy
48
49 states characteristic of a V_{Ag} created inside $[\text{AgO}_4]$ and $[\text{AgO}_2]$ clusters, respectively.
50
51
52
53
54
55
56
57
58
59
60

<Figure 3>

Figure 3. Positron wavefunction isodensities calculated for monovacancy states: **(A)** a V_O created between one $[\text{WO}_6]$ and one $[\text{AgO}_4]$ clusters; **(B)** a V_W created inside a $[\text{WO}_6]$ cluster; **(C)** a V_{Ag} formed inside an $[\text{AgO}_4]$ cluster; and **(D)** a V_{Ag} created within an $[\text{AgO}_2]$ cluster. The positron isodensities are represented by three surface contours, which correspond to 70%, 50% and 30% of the maximum positron density. For the sake of clarity, only the participating clusters are shown in the figures. W atoms are represented in red, Ag atoms in blue and O atoms in dark gray. Missing atoms related to the different monovacancies are labeled.

On the other hand, when oxygen vacancies are aggregated to a V_{Ag} to form different Ag-O vacancy complexes (*i.e.*, one V_{Ag} complex with one or more oxygen vacancies), the related positron lifetimes are higher than those calculated for the positron annihilated in a V_{Ag} ($\sim 10\%$ and $\sim 20\%$ for Ag-O divacancy and Ag-O trivacancy, respectively), meaning that these complexes are deeper positron traps. **Figs. 4(A), 4(B)** and **4(C)** display positron wavefunction isodensity plots calculated for the vacancy complexes representing a $V_{Ag} + V_O$ divacancy created inside an $[\text{AgO}_2]$ cluster, a $V_{Ag} + 2V_O$ trivacancy corresponding to the whole missing $[\text{AgO}_2]$ cluster, and a $V_{Ag} + 2V_O$ trivacancy formed inside an $[\text{AgO}_4]$ cluster, respectively. In the case of V_{Ag} , the positron wavefunction is strongly localized inside the Ag vacancy and the corresponding positron wave function isodensities are slightly affected by the presence of V_O . Finally, important changes in the positron parameters regarding the $2V_{Ag} + 4V_O$ hexavacancy were observed. We could note that the presence of a second V_{Ag} reduces the positron lifetime and the corresponding E_b values, strongly modifying the positron wavefunction,

1
2
3 according to the isodensity plot presented in **Fig. 4(D)**, where it is possible to see the
4
5 positron localized between two Ag vacancies.
6
7
8
9

10 <Figure 4>

11
12 **Figure 4.** Positron wavefunction isodensities calculated for vacancy complexes: **(A)** a
13 $V_{Ag} + V_O$ divacancy created inside an $[AgO_2]$ cluster; **(B)** a $V_{Ag} + 2V_O$ trivacancy
14 corresponding to the whole missing $[AgO_2]$ cluster; **(C)** a $V_{Ag} + 2V_O$ trivacancy formed
15 inside an $[AgO_4]$ cluster; and **(D)** a $2V_{Ag} + 4V_O$ hexavacancy created between an $[AgO_2]$
16 cluster and a neighboring $[AgO_7]$ cluster. The positron isodensities are represented by
17 three surface contours, which correspond to 70%, 50% and 30% of the maximum
18 positron density within the contour. For the sake of clarity, only the participating
19 clusters are shown in the figures. W atoms are represented in red, Ag atoms in blue and
20 O atoms in dark gray. Missing atoms related to the different monovacancies forming the
21 vacancy complexes are labeled.
22
23
24
25
26
27
28
29
30
31
32
33
34
35
36
37

38 Based on the lifetime values obtained by first-principles calculations, the experimental
39 results reported in **Tables 1 and 2** can be rationalized as follows:

40
41 - For the WT samples: The shortest lifetime τ_1 is always lower than the calculated τ_b . In
42 such a case, τ_1 must be considered as a reduced bulk lifetime due to positron
43 annihilation in intragranular defects characterized by the second lifetime component.
44 Therefore, the relevant information linked to vacancy-like defects can be obtained from
45 τ_2 and I_2 . For the non-irradiated sample, $\tau_2 = 274 \pm 2$ ps and $I_2 \sim 73\%$. Taking into account
46 the calculated positron lifetimes reported in **Table 3**, the experimental τ_2 value can be
47 interpreted as the result of positron annihilations in Ag-O vacancy complexes.
48 Specifically, positron traps have a size distribution around a mean value equivalent to
49
50
51
52
53
54
55
56
57
58
59
60

1
2
3 that formed by two oxygen vacancies surrounding one silver vacancy ($V_{Ag} + 2V_O$).
4
5 Besides, the elevated I_2 value indicates a high concentration of this kind of defect in the
6
7 non-irradiated sample. When the EBI exposure time increases, the τ_2 values decrease
8
9 from 274 to 263 ps, while the associated I_2 values increase from $\sim 73\%$ to $\sim 80\%$. The
10
11 change in the positron lifetime can be assigned to a progressive decrease in the
12
13 concentration of Ag-O vacancy complexes (greater than $V_{Ag} + 2V_O$) with a consequent
14
15 increase in the concentration of a smaller type of vacancies such as V_{Ag} and $V_{Ag} + V_O$. It
16
17 is worth mentioning that the I_2 increases reflect an increment of the total concentration
18
19 of defects related to silver vacancies.
20
21
22
23

24 - For the AL samples: The interpretation of the experimental positron lifetimes reported
25
26 in **Table 2** requires a different sequence when compared with the results obtained for
27
28 the irradiated and non-irradiated WT samples. First, all τ_2 and I_2 values are respectively
29
30 higher and lower than those obtained for the WT samples. Regarding the τ_2
31
32 experimental value, it is higher than the maximum theoretical lifetime calculated for the
33
34 different defect states listed in **Table 3**. As a consequence, it must be assumed that
35
36 positrons are annihilated in vacancy complexes (VC) containing Ag vacancies ($Ag-VC$)
37
38 with an associated open volume larger than that of a $2V_{Ag} + 4V_O$ hexavacancy. In order
39
40 to obtain higher theoretical positron lifetimes, it is necessary to build more complex
41
42 structures of vacancy clusters that should be associated with real defects. For our
43
44 calculations, we tried to avoid building defects that could be hardly interpreted in terms
45
46 of a feasible defect structure. On the other hand, increased EBI exposure times decrease
47
48 the systematic τ_2 , which in turn is correlated with a strong increase of I_2 . This behavior
49
50 could be interpreted as a progressive decrease in the VC concentration with a
51
52 consequent increase in the concentration of Ag-O vacancy complexes having an
53
54 equivalent mean size between a $V_{Ag} + 2V_O$ trivacancy and a $2V_{Ag} + 4V_O$ hexavacancy.
55
56
57
58
59
60

1
2
3 As it can be seen in **Table 2**, when the irradiation times increase, the τ_I and I_I values
4 systematically decrease from ~ 219 to ~ 178 ps and from $\sim 61\%$ to $\sim 25\%$, respectively.
5

6
7 To simplify the interpretation of the PALS results obtained for the AL samples, the data
8 obtained by measuring the samples submitted to the maximum EBI time (9 min) are
9 firstly presented and discussed. At this irradiation time, the experimental τ_I value is,
10 within the error bars, equal to the calculated lifetime τ_b , and its associated intensity is
11 non-negligible ($I_I \sim 25\%$). Consequently, it can be concluded that a shorter lifetime is an
12 average positron lifetime, resulting from the contributions of the reduced bulk positron
13 lifetime and those coming from positron annihilations in V_{Ag} . Thus, in terms of the
14 theoretical positron lifetimes reported in **Table 3**, by decreasing the EBI exposure times
15 the τ_I tends to increase, which can be mainly assigned to a significant and systematic
16 increase in positron annihilability in V_{Ag} .
17
18
19
20
21
22
23
24
25
26
27
28
29
30
31
32

33 **4. CONCLUSIONS**

34 Information on the type and concentration of defects and the localization of their
35 electronic levels in the semiconductor oxides is critical to design materials with specific
36 characteristics to be used in different technological applications. In particular, it is
37 essential to understand the changes in the structural defects at nano- and sub-
38 nanometric scales as a consequence of the modification of materials due to EBI.
39

40 A detailed analysis based on the results obtained by positron annihilation lifetime
41 spectroscopy together with the theoretical positron lifetime values calculated using first-
42 principle calculations at the DFT level made it possible to establish the nature of
43 vacancy-like defects in both pure $\alpha\text{-Ag}_2\text{WO}_4$ samples and those submitted to EBI. The
44 PL measurements revealed that the increase of EBI exposure time induces a progressive
45 change in the defect structure from shallow vacancy defects to deep ones.
46
47
48
49
50
51
52
53
54
55
56
57
58
59
60

1
2
3 The main conclusions of the present work can be summarized as follows: i) for non-
4 irradiated α - Ag_2WO_4 samples synthesized in water, the defects are mainly composed of
5
6 a high concentration of Ag-O vacancy complexes with a mean size equivalent to a
7
8 trivacancy formed by two V_O surrounding one Ag vacancy; (ii) the defects in the non-
9
10 irradiated α - Ag_2WO_4 samples synthesized in ethanol mainly comprise an Ag vacancy
11
12 complemented with a non-negligible concentration of vacancy clusters containing three
13
14 or more V_{Ag} ; (iii) in the irradiated samples synthesized in water, we observed that an
15
16 increase of the EBI exposure times causes a larger progressive decrease in the
17
18 concentration of Ag-O vacancy complexes than a trivacancy with concomitant increase
19
20 in the concentration of V_{Ag} and Ag-O divacancies. In addition, a slight increase in the
21
22 total concentration of defects related to V_{Ag} was detected. In these samples, the
23
24 irradiation induced the formation of new small Ag-related defects; finally, (iv) for the
25
26 irradiated samples synthesized in ethanol, the increase of irradiation times induces a
27
28 progressive decrease in the concentration of vacancy clusters containing Ag vacancies
29
30 with concomitant formation of an important number of Ag-O vacancy complexes bigger
31
32 than a $V_{Ag} + 2V_O$ trivacancy.
33
34
35
36
37
38
39

40 The present results have provided a complete defect structural description of pure α -
41
42 Ag_2WO_4 semiconductor under EBI that would contribute to the better control of its
43
44 tunable response. It is not only related to the formation of quantum dots, which confine
45
46 the electrons at the Ag vacancy centers, but also provides unambiguous physical
47
48 meaning on the nature of defects generated by EBI. The knowledge gained by this study
49
50 can allow engineers to incorporate new functionalities into Ag_2WO_4 -based
51
52 semiconductor devices.
53
54
55
56
57
58

59 CONFLITS OF INTEREST

60

1
2
3 There are no conflicts to declare.
4
5
6

7 **ACKNOWLEDGMENTS**

9 This work was partly funded by the Fundação de Amparo à Pesquisa do Estado de São
10 Paulo – FAPESP (grants No. 2013/07296-2 and 2019/01732-1), the Financiadora de
11 Estudos e Projetos – FINEP, Conselho Nacional de Desenvolvimento Científico e
12 Tecnológico – CNPq (grants No. 166281/2017-4 and 426634/2018-7) and the
13 Coordenação de Aperfeiçoamento de Pessoal de Nível Superior CAPES. J.A.
14 acknowledges Universitat Jaume I (project UJI-B2019-30), and the Ministerio de
15 Ciencia, Innovación y Universidades (Spain (Spain) (project PGC2018094417-B-I00)
16 for financially supporting this research. C.M. and A.S. thank the funding from the
17 Agencia Nacional de Promoción Científica y Tecnológica – ANPCyT (Argentina)
18 (PICT 2015-1832), the Comisión de Investigaciones Científicas de la Provincia de
19 Buenos Aires – CICPBA (Argentina) and the Secretaría de Ciencia, Arte y Tecnología,
20 UNCPBA (Argentina).
21
22
23
24
25
26
27
28
29
30
31
32
33
34
35
36
37
38

39 **REFERENCES**

- 40
41
42
43
44 (1) Alkauskas, A.; McCluskey, M. D.; Van de Walle, C. G. Tutorial: Defects in
45 Semiconductors - Combining Experiment and Theory. *J. Appl. Phys.* **2016**, *119*,
46 181101. <https://doi.org/10.1063/1.4948245>.
47
48
49
50
51 (2) Park, J.-S.; Kim, S.; Xie, Z.; Walsh, A. Point Defect Engineering in Thin-Film
52 Solar Cells. *Nat. Rev. Mater.* **2018**, *3*, 194. [https://doi.org/10.1038/s41578-018-](https://doi.org/10.1038/s41578-018-0026-7)
53 [0026-7](https://doi.org/10.1038/s41578-018-0026-7).
54
55
56
57
58 (3) Bassett, L. C.; Alkauskas, A.; Exarhos, A. L.; Fu, K.-M. C. Quantum Defects by
59 Design. *Nanophotonics*. **2019**, 1867. <https://doi.org/10.1515/nanoph-2019-0211>.
60

- 1
2
3 (4) Stoneham, A. M. *Theory of Defects in Solids: Electronic Structure of Defects in*
4 *Insulators and Semiconductors*; Oxford University Press: Oxford, **2001**.
5
6 <https://doi.org/10.1093/acprof:oso/9780198507802.001.0001>.
7
8
9
10 (5) Baranowski, L. L.; Zawadzki, P.; Lany, S.; Toberer, E. S.; Zakutayev, A. A
11 Review of Defects and Disorder in Multinary Tetrahedrally Bonded
12 Semiconductors. *Semicond. Sci. Technol.* **2016**, *31*, 123004.
13
14 <https://doi.org/10.1088/0268-1242/31/12/123004>.
15
16
17
18 (6) Chapter V - Defects. In *CdTe and Related Compounds; Physics, Defects, Hetero-*
19 *and Nano-structures, Crystal Growth, Surfaces and Applications*; Triboulet, R.,
20 Siffert, P., Eds.; European Materials Research Society Series; Elsevier:
21 Amsterdam, **2010**; 169-221. [https://doi.org/https://doi.org/10.1016/B978-0-08-](https://doi.org/https://doi.org/10.1016/B978-0-08-046409-1.00005-8)
22 [046409-1.00005-8](https://doi.org/https://doi.org/10.1016/B978-0-08-046409-1.00005-8).
23
24
25
26 (7) Ran, C.; Xu, J.; Gao, W.; Huang, C.; Dou, S. Defects in Metal Triiodide
27 Perovskite Materials towards High-Performance Solar Cells: Origin, Impact,
28 Characterization, and Engineering. *Chem. Soc. Rev.* **2018**, *47*, 4581–4610.
29
30 <https://doi.org/10.1039/C7CS00868F>.
31
32
33 (8) Sholl, D. S.; Lively, R. P. Defects in Metal–Organic Frameworks: Challenge or
34 Opportunity? *J. Phys. Chem. Lett.* **2015**, *6*, 3437–3444.
35
36 <https://doi.org/10.1021/acs.jpcllett.5b01135>.
37
38
39 (9) Chen, F.-M.; Liu, X. Advancing Biomaterials of Human Origin for Tissue
40 Engineering. *Prog. Polym. Sci.* **2016**, *53*, 86–168.
41
42 <https://doi.org/10.1016/j.progpolymsci.2015.02.004>.
43
44
45 (10) Samarth, N. Quantum Materials Discovery from a Synthesis Perspective. *Nat.*
46 *Mater.* **2017**, *16*, 1068–1076. <https://doi.org/10.1038/nmat5010>.
47
48
49 (11) de Quilettes, D. W.; Vorpahl, S. M.; Stranks, S. D.; Nagaoka, H.; Eperon, G. E.;
50
51
52
53
54
55
56
57
58
59
60

- 1
2
3 Ziffer, M. E.; Snaith, H. J.; Ginger, D. S. Impact of Microstructure on Local
4 Carrier Lifetime in Perovskite Solar Cells. *Science*. **2015**, *348*, 683 – 686.
5
6 <https://doi.org/10.1126/science.aaa5333>.
7
8
9
10 (12) Heo, S.; Seo, G.; Lee, Y.; Lee, D.; Seol, M.; Lee, J.; Park, J.-B.; Kim, K.; Yun,
11 D.-J.; Kim, Y. S.; et al. Deep Level Trapped Defect Analysis in CH₃NH₃PbI₃
12 Perovskite Solar Cells by Deep Level Transient Spectroscopy. *Energy Environ.*
13 *Sci.* **2017**, *10*, 1128–1133. <https://doi.org/10.1039/C7EE00303J>.
14
15
16
17
18
19 (13) Lu, I.-T.; Bernardi, M. Using Defects to Store Energy in Materials – a
20 Computational Study. *Sci. Rep.* **2017**, *7*, 3403. [https://doi.org/10.1038/s41598-](https://doi.org/10.1038/s41598-017-01434-8)
21 [017-01434-8](https://doi.org/10.1038/s41598-017-01434-8).
22
23
24
25
26 (14) Hautojärvi, P.; Corbel, C. Positron Spectroscopy of Defects in Metals and
27 Semiconductors, in Positron Spectroscopy of Solids; Dupasquier, A., Mills Jr., A.
28 P., Eds.; IOS Press: Amsterdam, 1995.
29
30
31
32
33 (15) Tuomisto, F.; Makkonen, I. Defect Identification in Semiconductors with
34 Positron Annihilation: Experiment and Theory. *Rev. Mod. Phys.* **2013**, *85*, 1583–
35 1631. <https://doi.org/10.1103/RevModPhys.85.1583>.
36
37
38
39
40 (16) Krause-Rehberg, R.; Leipner, H. S. *Positron Annihilation in Semiconductors:*
41 *Defect Studies*; Springer Science & Business Media, 1999.
42
43
44
45 (17) Tuomisto, F.; Ranki, V.; Saarinen, K.; Look, D. C. Evidence of the Zn Vacancy
46 Acting as the Dominant Acceptor in n-Type ZnO. *Phys. Rev. Lett.* **2003**, *91*,
47 205502. <https://doi.org/10.1103/PhysRevLett.91.205502>.
48
49
50
51 (18) Makkonen, I.; Korhonen, E.; Prozheeva, V.; Tuomisto, F. Identification of
52 Vacancy Defect Complexes in Transparent Semiconducting Oxides ZnO, In₂O₃
53 and SnO₂. *J. Phys. Condens. Matter* **2016**, *28*, 224002.
54
55
56
57
58
59
60 <https://doi.org/10.1088/0953-8984/28/22/224002>.

- 1
2
3 (19) Brauer, G.; Anwand, W.; Skorupa, W.; Kuriplach, J.; Melikhova, O.; Moisson,
4 C.; von Wenckstern, H.; Schmidt, H.; Lorenz, M.; Grundmann, M. Defects in
5 Virgin and N-Implanted ZnO Single Crystals Studied by Positron Annihilation,
6 Hall Effect, and Deep-Level Transient Spectroscopy. *Phys. Rev. B* **2006**, *74*,
7 45208. <https://doi.org/10.1103/PhysRevB.74.045208>.
8
9
10
11
12
13
14 (20) Shek, C. H.; Lai, J. K. L.; Lin, G. M. Investigation of Interface Defects in
15 Nanocrystalline SnO₂ by Positron Annihilation. *J. Phys. Chem. Solids* **1999**, *60*,
16 189–193. [https://doi.org/10.1016/S0022-3697\(98\)00269-8](https://doi.org/10.1016/S0022-3697(98)00269-8).
17
18
19
20
21 (21) Guagliardo, P. R.; Vance, E. R.; Zhang, Z.; Davis, J.; Williams, J. F.; Samarin, S.
22 N. Positron Annihilation Lifetime Studies of Nb-Doped TiO₂, SnO₂, and ZrO₂.
23 *J. Am. Ceram. Soc.* **2012**, *95*, 1727–1731. [https://doi.org/10.1111/j.1551-](https://doi.org/10.1111/j.1551-2916.2012.05157.x)
24 [2916.2012.05157.x](https://doi.org/10.1111/j.1551-2916.2012.05157.x).
25
26
27
28
29
30 (22) Čížek J., Melikhova, O.; Procházka, I.; Kuriplach, J.; Kužel, R.; Brauer, G.;
31 Anwand, W.; Konstantinova, T. E.; Danilenko, I. A. Defect Studies of
32 Nanocrystalline Zirconia Powders and Sintered Ceramics. *Phys. Rev. B* **2010**, *81*,
33 24116. <https://doi.org/10.1103/PhysRevB.81.024116>.
34
35
36
37
38
39 (23) Ponce, M. A.; Macchi, C.; Schipani, F.; Aldao, C. M.; Somoza, A. Mild
40 Degradation Processes in ZnO-Based Varistors: The Role of Zn Vacancies.
41 *Philos. Mag.* **2015**, *95*, 730–743.
42 <https://doi.org/10.1080/14786435.2015.1006291>.
43
44
45
46
47
48 (24) Macchi, C.; Ponce, M. A.; Desimone, P. M.; Aldao, C. M.; Somoza, A. Vacancy-
49 like Defects in Nanocrystalline SnO₂: Influence of the Annealing Treatment
50 under Different Atmospheres. *Philos. Mag.* **2018**, *98*, 673–692.
51 <https://doi.org/10.1080/14786435.2017.1415466>.
52
53
54
55
56
57 (25) Saarinen, K.; Hautojärvi, P.; Corbel, C. Chapter 5 Positron Annihilation
58
59
60

- 1
2
3 Spectroscopy of Defects in Semiconductors. In *Identification of Defects in*
4 *Semiconductors*; Stavola, M. B. T.-S. and S., Ed.; Elsevier, 1998; Vol. 51, 209–
5 285. [https://doi.org/10.1016/S0080-8784\(08\)63057-4](https://doi.org/10.1016/S0080-8784(08)63057-4).
6
7
8
9
10 (26) Wang, B.-Y.; Zhang, G.-Y.; Cui, G.-W.; Xu, Y.-Y.; Liu, Y.; Xing, C.-Y.
11 Controllable Fabrication of α -Ag₂WO₄ Nanorod-Clusters with Superior
12 Simulated Sunlight Photocatalytic Performance. *Inorg. Chem. Front.* **2019**, *6*,
13 209–219. <https://doi.org/10.1039/C8QI01025K>.
14
15
16
17
18 (27) Longo, E.; Cavalcante, L. S.; Volanti, D. P.; Gouveia, A. F.; Longo, V. M.;
19 Varela, J. A.; Orlandi, M. O.; Andrés, J. Direct in Situ Observation of the
20 Electron-Driven Synthesis of Ag Filaments on α -Ag₂WO₄ Crystals. *Sci. Rep.*
21 **2013**, *3*, 4–7. <https://doi.org/10.1038/srep01676>.
22
23
24
25
26
27
28 (28) Longo, E.; Volanti, D. P.; Nogueira, C.; Longo, M.; Gracia, L.; Almeida, M. a P.;
29 Pinheiro, A. N.; Ferrer, M. M.; Cavalcante, S.; Luis, R. W. Toward an
30 Understanding of the Growth of Ag Filaments on α - Ag₂WO₄ and Their
31 Photoluminescent Properties : A Combined Experimental and Theoretical Study.
32 *J. Phys. Chem. C* **2014**, *118*, 1229. <https://doi.org/10.1021/jp408167v>.
33
34
35
36
37
38
39 (29) Sczancoski, J. C.; Maya-Johson, S.; Da Silva Pereira, W.; Longo, E.; Leite, E. R.
40 Atomic Diffusion Induced by Electron-Beam Irradiation: An in Situ Study of Ag
41 Structures Grown from α -Ag₂WO₄. *Cryst. Growth Des.* **2019**, *19*, 106–115.
42 <https://doi.org/10.1021/acs.cgd.8b01076>.
43
44
45
46
47
48 (30) Lingerfelt, D. B.; Ganesh, P.; Jakowski, J.; Sumpter, B. G. Understanding Beam-
49 Induced Electronic Excitations in Materials. *J. Chem. Theory Comput.* **2020**, *16*,
50 1200–1214. <https://doi.org/10.1021/acs.jctc.9b00792>.
51
52
53
54
55 (31) Zhang, Q.; Li, H.; Gan, L.; Ma, Y.; Golberg, D.; Zhai, T. In Situ Fabrication and
56 Investigation of Nanostructures and Nanodevices with a Microscope. *Chem. Soc.*
57
58
59
60

- 1
2
3 *Rev.* **2016**, *45*, 2694–2713. <https://doi.org/10.1039/C6CS00161K>.
- 4
5 (32) Krasheninnikov, A. V; Nordlund, K. Ion and Electron Irradiation-Induced Effects
6 in Nanostructured Materials. *J. Appl. Phys.* **2010**, *107*, 71301.
7
8 <https://doi.org/10.1063/1.3318261>.
- 9
10 (33) Lin, F.; Markus, I. M.; Doeff, M. M.; Xin, H. L. Chemical and Structural
11 Stability of Lithium-Ion Battery Electrode Materials under Electron Beam. *Sci.*
12 *Rep.* **2014**, *4*, 5694. <https://doi.org/10.1038/srep05694>.
- 13
14 (34) Wei, B.; Lu, X.; Voisard, F.; Wei, H.; Chiu, H.; Ji, Y.; Han, X.; Trudeau, M. L.;
15 Zaghbi, K.; Demopoulos, G. P.; et al. In Situ TEM Investigation of Electron
16 Irradiation Induced Metastable States in Lithium-Ion Battery Cathodes:
17 Li₂FeSiO₄ versus LiFePO₄. *ACS Appl. Energy Mater.* **2018**, *1*, 3180–3189.
18
19 <https://doi.org/10.1021/acsaem.8b00391>.
- 20
21 (35) Li, X.; Qi, J.; Zhang, Q.; Wang, Z.; Lu, S.; Zhang, Y. Investigation of Electron
22 Beam Detection Properties of ZnO Nanowire Based Back-to-Back Double
23 Schottky Diode. *RSC Adv.* **2014**, *4*, 12743–12747.
24
25 <https://doi.org/10.1039/C3RA47934J>.
- 26
27 (36) Gonzalez-Martinez, I. G.; Bachmatiuk, A.; Bezugly, V.; Kunstmann, J.;
28 Gemming, T.; Liu, Z.; Cuniberti, G.; Rummeli, M. H. Electron-Beam Induced
29 Synthesis of Nanostructures: A Review. *Nanoscale* **2016**, *8*, 11340–11362.
30
31 <https://doi.org/10.1039/C6NR01941B>.
- 32
33 (37) Li, J.; Leonard Deepak, F. In Situ Generation of Sub-10 Nm Silver Nanowires
34 under Electron Beam Irradiation in a TEM. *Chem. Commun.* **2020**, *56*, 4765–
35 4768. <https://doi.org/10.1039/D0CC00909A>.
- 36
37 (38) Winkler, R.; Fowlkes, J. D.; Rack, P. D.; Plank, H. 3D Nanoprinting via Focused
38 Electron Beams. *J. Appl. Phys.* **2019**, *125*, 210901.
- 39
40
41
42
43
44
45
46
47
48
49
50
51
52
53
54
55
56
57
58
59
60

- 1
2
3 <https://doi.org/10.1063/1.5092372>.
- 4
5
6 (39) Assis, M.; Robeldo, T.; Foggi, C. C.; Kubo, A. M.; Mínguez-Vega, G.;
7 Condoncillo, E.; Beltran-Mir, H.; Torres-Mendieta, R.; Andrés, J.; Oliva, M.; et
8 al. Ag Nanoparticles/ α -Ag₂WO₄ Composite Formed by Electron Beam and
9 Femtosecond Irradiation as Potent Antifungal and Antitumor Agents. *Sci. Rep.*
10 **2019**, *9*, 9927. <https://doi.org/10.1038/s41598-019-46159-y>.
11
12
13
14
15
16
17 (40) Assis, M.; Condoncillo, E.; Torres-Mendieta, R.; Beltrán-Mir, H.; Mínguez-Vega,
18 G.; Oliveira, R.; Leite, E. R.; Foggi, C. C.; Vergani, C. E.; Longo, E.; et al.
19 Towards the Scale-up of the Formation of Nanoparticles on α -Ag₂WO₄ with
20 Bactericidal Properties by Femtosecond Laser Irradiation. *Sci. Rep.* **2018**, *8*, 1–
21 11. <https://doi.org/10.1038/s41598-018-19270-9>.
22
23
24
25
26
27
28 (41) Zhang, R, Cui H, Yang X, Tang H, Liu H, Li Y. Facile hydrothermal synthesis
29 and photocatalytic activity of rod-like nanosized silver tungstate. *Micro & Nano*
30 *Letters.* **2012**, *7*, 1285-1288. <https://doi.org/10.1049/mnl.2012.0765>
31
32
33
34
35 (42) Chen, H., Xu, Y. Photoactivity and Stability of Ag₂WO₄ for Organic
36 Degradation in Aqueous Suspensions. *Appl. Surf. Sci.* **2014**, *319*, 319–323.
37 <https://doi.org/10.1016/j.apsusc.2014.05.115>
38
39
40
41
42 (43) Liu, D.; Huang, W.; Li, L.; Liu, L.; Sun, X.; Liu, B.; Yang, B.; Guo, C.
43 Experimental and Theoretical Investigation on Photocatalytic Activities of 1D
44 Ag/Ag₂WO₄ Nanostructures. *Nanotechnology* **2017**, *28*, 385702.
45 <https://doi.org/10.1088/1361-6528/aa7d96>.
46
47
48
49
50
51 (44) Longo, V. M.; De Foggi, C. C.; Ferrer, M. M.; Gouveia, A. F.; André, R. S.;
52 Avansi, W.; Vergani, C. E.; Machado, A. L.; Andrés, J.; Cavalcante, L. S.; et al.
53 Potentiated Electron Transference in α -Ag₂WO₄ Microcrystals with Ag
54 Nanofilaments as Microbial Agent. *J. Phys. Chem. A* **2014**, *118*, 5769–5778.
55
56
57
58
59
60

- 1
2
3 <https://doi.org/10.1021/jp410564p>.
- 4
5 (45) de Foggi, C. C.; de Oliveira, R. C.; Fabbro, M. T.; Vergani, C. E.; Andres, J.;
6 Longo, E.; Machado, A. L. Tuning the Morphological, Optical, and
7 Antimicrobial Properties of α -Ag₂WO₄ Microcrystals Using Different Solvents.
8 *Cryst. Growth Des.* **2017**, *17*, 6239–6246.
9 <https://doi.org/10.1021/acs.cgd.7b00786>.
- 10
11 (46) Macedo, N. G.; Machado, T. R.; Roca, R. A.; Assis, M.; Foggi, C. C.; Puerto-
12 Belda, V.; Mínguez-Vega, G.; Rodrigues, A.; San-Miguel, M. A.; Cordoncillo, E.
13 Tailoring the Bactericidal Activity of Ag Nanoparticles/ α -Ag₂WO₄ Composite
14 Induced by Electron Beam and Femtosecond Laser Irradiation: Integration of
15 Experiment and Computational Modeling. *ACS Appl. Bio Mater.* **2019**, *2*, 824–
16 837. <https://doi.org/10.1021/acsabm.8b00673>.
- 17
18 (47) De Foggi, C. C.; De Oliveira, R. C.; Assis, M.; Fabbro, M. T.; Mastelaro, V. R.;
19 Vergani, C. E.; Gracia, L.; Andrés, J.; Longo, E.; Machado, A. L. Unveiling the
20 Role of β -Ag₂MoO₄ Microcrystals to the Improvement of Antibacterial Activity.
21 *Mater. Sci. Eng. C* **2020**, 110765.
22 <https://doi.org/https://doi.org/10.1016/j.msec.2020.110765>.
- 23
24 (48) Pereira, W. da S.; Andrés, J.; Gracia, L.; San-Miguel, M. A.; da Silva, E. Z.;
25 Longo, E.; Longo, V. M. Elucidating the Real-Time Ag Nanoparticle Growth on
26 α -Ag₂WO₄ during Electron Beam Irradiation: Experimental Evidence and
27 Theoretical Insights. *Phys. Chem. Chem. Phys.* **2015**, *17*, 5352–5359.
28 <https://doi.org/10.1039/C4CP05849F>.
- 29
30 (49) San-Miguel, M. A.; Da Silva, E. Z.; Zanetti, S. M.; Cilense, M.; Fabbro, M. T.;
31 Gracia, L.; Andrés, J.; Longo, E. In Situ Growth of Ag Nanoparticles on α -
32 Ag₂WO₄ under Electron Irradiation: Probing the Physical Principles.
33
34
35
36
37
38
39
40
41
42
43
44
45
46
47
48
49
50
51
52
53
54
55
56
57
58
59
60

- 1
2
3 *Nanotechnology* **2016**, *27*, 225703. <https://doi.org/10.1088/0957->
4
5 4484/27/22/225703.
6
7
8 (50) Andrés, J.; Gracia, L.; Gonzalez-Navarrete, P.; Longo, V. M.; Avansi, W.;
9
10 Volanti, D. P.; Ferrer, M. M.; Lemos, P. S.; La Porta, F. A.; Hernandez, A. C.; et
11
12 al. Structural and Electronic Analysis of the Atomic Scale Nucleation of Ag on α -
13
14 Ag₂WO₄ Induced by Electron Irradiation. *Sci. Rep.* **2014**, *4*, 1–7.
15
16 <https://doi.org/10.1038/srep05391>.
17
18
19 (51) Longo, E.; Avansi, W.; Bettini, J.; Andrés, J.; Gracia, L. In Situ Transmission
20
21 Electron Microscopy Observation of Ag Nanocrystal Evolution by Surfactant
22
23 Free Electron-Driven Synthesis. *Sci. Rep.* **2016**, *6* (1), 21498.
24
25 <https://doi.org/10.1038/srep21498>.
26
27
28 (52) Andrés, J.; Ferrer, M. M.; Gracia, L.; Beltran, A.; Longo, V. M.; Cruvinel, G. H.;
29
30 Tranquilin, R. L.; Longo, E. A Combined Experimental and Theoretical Study on
31
32 the Formation of Ag Filaments on β -Ag₂MoO₄ Induced by Electron Irradiation.
33
34 *Part. Part. Syst. Charact.* **2015**, *32* (6), 646–651.
35
36 <https://doi.org/10.1002/ppsc.201400162>.
37
38
39 (53) Lemos, P. S.; Silva, G., S.; Roca, R. A.; Assis, M.; Torre-Mendieta, R.; Beltran-
40
41 Mir, H.; Minguez-Vega, G.; Cordoncillo, E.; Andrés, J.; Longo, E.. Laser and
42
43 Electron Beam-Induced Formation of Ag/Cr Structures on Ag₂CrO₄. *Phys.*
44
45 *Chem. Chem. Phys.* **2019**, *21* (11), 6101–6111.
46
47 <https://doi.org/10.1039/C8CP07263A>.
48
49
50 (54) Assis, M.; Carvalho de Oliveira, M.; Machado, T. R.; Macedo, N. G.; Costa, J. P.
51
52 C.; Gracia, L.; Andrés, J.; Longo, E. In Situ Growth of Bi Nanoparticles on
53
54 NaBiO₃, δ -, and β -Bi₂O₃ Surfaces: Electron Irradiation and Theoretical Insights.
55
56 *J. Phys. Chem. C* **2019**, *123*, 5023–5030.
57
58
59
60

- 1
2
3 <https://doi.org/10.1021/acs.jpcc.8b11566>.
- 4
5 (55) Assis, M.; Pontes Ribeiro, R. A.; Carvalho, M. H.; Teixeira, M. M.; Gobato, Y.
6 G.; Prando, G. A.; Mendonça, C. R.; de Boni, L.; Aparecido de Oliveira, A. J.;
7 Bettini, J.; et al. Unconventional Magnetization Generated from Electron Beam
8 and Femtosecond Irradiation on α -Ag₂WO₄: A Quantum Chemical Investigation.
9 *ACS Omega* **2020**, *5*, 10052–10067. <https://doi.org/10.1021/acsomega.0c00542>.
- 10
11 (56) Kansy, J. Microcomputer Program for Analysis of Positron Annihilation Lifetime
12 Spectra. *Nucl. Instruments Methods Phys. Res. Sect. A Accel. Spectrometers,*
13 *Detect. Assoc. Equip.* **1996**, *374*, 235–244. [https://doi.org/10.1016/0168-](https://doi.org/10.1016/0168-9002(96)00075-7)
14 [9002\(96\)00075-7](https://doi.org/10.1016/0168-9002(96)00075-7).
- 15
16 (57) Furthmüller, J.; Kresse, G. Efficiency of Ab-Initio Total Energy Calculations for
17 Metals and Semiconductors Using a Plane-Wave Basis Set. *Computational*
18 *Materials Science.* 1996, 15–50. [https://doi.org/10.1016/0927-0256\(96\)00008-0](https://doi.org/10.1016/0927-0256(96)00008-0).
- 19
20 (58) Kresse, G.; Hafner, J. Ab Initio Molecular-Dynamics Simulation of the Liquid-
21 Metal–Amorphous-Semiconductor Transition in Germanium. *Phys. Rev. B* **1994**,
22 *49*, 14251–14269. <https://doi.org/10.1103/PhysRevB.49.14251>.
- 23
24 (59) Perdew, J. P.; Burke, K.; Ernzerhof, M.; of Physics, D.; Quantum Theory Group
25 Tulane University, N. O. L. 70118 J. Generalized Gradient Approximation Made
26 Simple. *Phys. Rev. Lett.* **1996**, *77*, 3865–3868.
27 <https://doi.org/10.1103/PhysRevLett.77.3865>.
- 28
29 (60) Kresse, G. From Ultrasoft Pseudopotentials to the Projector Augmented-Wave
30 Method. *Phys. Rev. B* **1999**, *59*, 1758–1775.
31 <https://doi.org/10.1103/PhysRevB.59.1758>.
- 32
33 (61) Macchi, C.; Maurizio, C.; Checchetto, R.; Mariazzi, S.; Ravelli, L.; Egger, W.;
34 Mengucci, P.; Bazzanella, N.; Miotello, A.; Somoza, A.; et al. Niobium
35
36
37
38
39
40
41
42
43
44
45
46
47
48
49
50
51
52
53
54
55
56
57
58
59
60

- 1
2
3 Aggregation and Vacancylike Defect Evolution in Nanostructured Nb-Doped
4
5 Mg: Their Role in the Kinetics of the Hydride-to-Metal Phase Transformation.
6
7 *Phys. Rev. B* **2012**, *85*, 214117. <https://doi.org/10.1103/PhysRevB.85.214117>.
8
9
- (62) Puska, M. J.; Mäkinen, S.; Manninen, M.; Nieminen, R. M. Screening of
10
11 Positrons in Semiconductors and Insulators. *Phys. Rev. B* **1989**, *39*, 7666–7679.
12
13 <https://doi.org/10.1103/PhysRevB.39.7666>.
14
15
- (63) Torsti, T.; Eirola, T.; Enkovaara, J.; Hakala, T.; Havu, P.; Havu, V.;
16
17 Höynälänmaa, T.; Ignatius, J.; Lyly, M.; Makkonen, I.; et al. Three Real-Space
18
19 Discretization Techniques in Electronic Structure Calculations. *Phys. status*
20
21 *solidi* **2006**, *243*, 1016–1053. <https://doi.org/10.1002/pssb.200541348>.
22
23
24
- (64) Boronski, E.; Nieminen, R. M. Electron-Positron Density-Functional Theory.
25
26 *Phys. Rev. B* **1986**, *34*, 3820–3831. <https://doi.org/10.1103/PhysRevB.34.3820>.
27
28
29
- (65) Macedo, N. G.; Gouveia, A. F.; Roca, R. A.; Assis, M.; Gracia, L.; Andrés, J.;
30
31 Leite, E. R.; Longo, E. Surfactant-Mediated Morphology and Photocatalytic
32
33 Activity of α -Ag₂WO₄ Material. *J. Phys. Chem. C* **2018**, *122*, 8667–8679.
34
35
36 <https://doi.org/10.1021/acs.jpcc.8b01898>.
37
38
- (66) Makkonen, I.; Puska, M. J. Energetics of Positron States Trapped at Vacancies in
39
40 Solids. *Phys. Rev. B* **2007**, *76*, 54119.
41
42
43 <https://doi.org/10.1103/PhysRevB.76.054119>.
44
45
- (67) Wiktor, J.; Barthe, M.-F.; Jomard, G.; Torrent, M.; Freyss, M.; Bertolus, M.
46
47 Coupled experimental and DFT+U investigation of positron lifetimes in UO₂.
48
49 *Phys. Rev. B* **2014**, *90* (18), 184101.
50
51
52 <https://doi.org/10.1103/PhysRevB.90.184101>.
53
54
- (68) Cavalcante, L. S.; Almeida, M. A. P.; Avansi, W.; Tranquilin, R. L.; Longo, E.;
55
56 Batista, N. C.; Mastelaro, V. R.; Li, M. S. Cluster Coordination and
57
58
59
60

- 1
2
3 Photoluminescence Properties of α -Ag₂WO₄ Microcrystals. *Inorg. Chem.* **2012**,
4
5 51, 10675–10687. <https://doi.org/10.1021/ic300948n>.
6
7
8 (69) Andres, J.; Longo, E.; Gouveia, A. F.; Gracia, L.; Oliveira, M. C. In Situ
9
10 Formation of Metal Nanoparticles through Electron Beam Irradiation: Modeling
11
12 Real Materials from First-Principles Calculations. *J. Mater. Sci. Eng.* **2018**, 07, .
13
14 <https://doi.org/10.4172/2169-0022.1000461>.
15
16
17 (70) Andrés, J.; Gouveia, A. F.; Gracia, L.; Longo, E.; Manzeppi Faccin, G.; da Silva,
18
19 E. Z.; Pereira, D. H.; San-Miguel, M. A. Formation of Ag Nanoparticles under
20
21 Electron Beam Irradiation: Atomistic Origins from First-principles Calculations.
22
23 *Int. J. Quantum Chem.* **2018**, 118, e25551. <https://doi.org/10.1002/qua.25551>
24
25
26 (71) Tang, J.; Ye, J. Correlation of Crystal Structures and Electronic Structures and
27
28 Photocatalytic Properties of the W-Containing Oxides. *J. Mater. Chem.* **2005**, 15,
29
30 4246–4251. <https://doi.org/10.1039/b504818d>.
31
32
33 (72) Tang, J.; Zou, Z.; Ye, J. Photophysical and Photocatalytic Properties of AgInW₂
34
35 O₈. *J. Phys. Chem. B* **2003**, 107, 14265–14269.
36
37 <https://doi.org/10.1021/jp0359891>.
38
39
40 (73) Sreedevi, A.; Priyanka, K. P.; Babitha, K. K.; Ganesh, S.; Varghese, T. Influence
41
42 of Electron Beam Irradiation on Structural and Optical Properties of Alpha
43
44 Ag₂WO₄. *Micron.* **2016**, 88, 1–6.
45
46 <https://doi.org/10.1016/j.radphyschem.2014.01.016>.
47
48
49 (74) Trudel, S. Unexpected Magnetism in Gold Nanostructures: Making Gold Even
50
51 More Attractive. *Gold Bull.* **2011**, 44, 3–13. [https://doi.org/10.1007/s13404-010-](https://doi.org/10.1007/s13404-010-0002-5)
52
53 0002-5.
54
55
56 (75) Longo, V. M.; De Figueiredo, A. T.; Campos, A. B.; Espinosa, J. W. M.;
57
58 Hernandez, A. C.; Taft, C. A.; Sambrano, J. R.; Varela, J. A.; Longo, E. Different
59
60

1
2
3 Origins of Green-Light Photoluminescence Emission in Structurally Ordered and
4 Disordered Powders of Calcium Molybdate. *J. Phys. Chem. A* **2008**, *112*, 8920–
5 8928. <https://doi.org/10.1021/jp801587w>.
6
7
8

- 9
10 (76) Zhang, F.; Yiu, Y.; Aronson, M. C.; Wong, S. S. Exploring the Room-
11 Temperature Synthesis and Properties of Multifunctional Doped Tungstate
12 Nanorods. *J. Phys. Chem. C* **2008**, *112*, 14816–14824.
13
14
15
16
17 <https://doi.org/10.1021/jp803611n>.
18
19
20
21
22
23
24
25
26
27
28
29
30
31
32
33
34
35
36
37
38
39
40
41
42
43
44
45
46
47
48
49
50
51
52
53
54
55
56
57
58
59
60

FIGURES AND TABLES

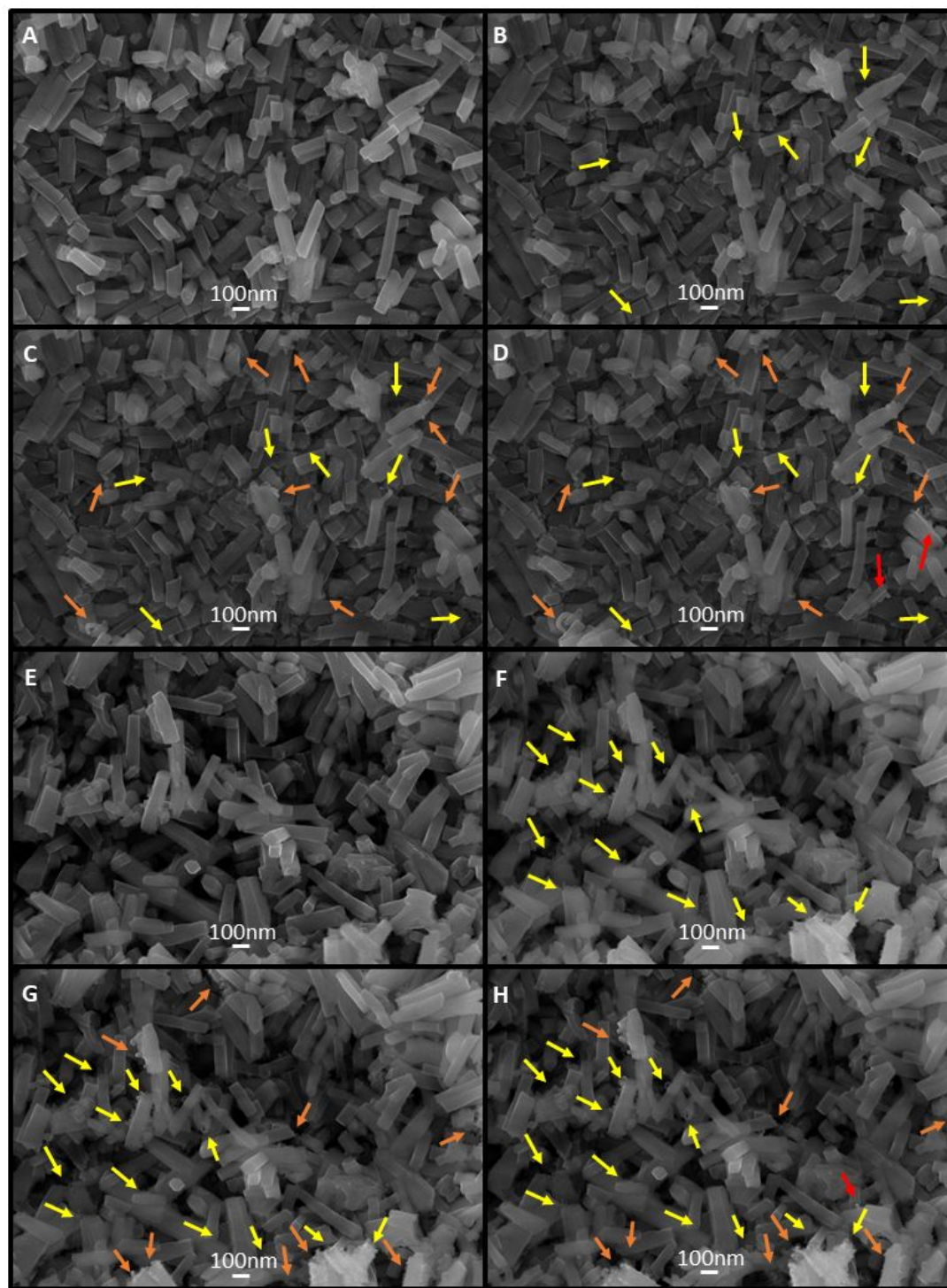


Figure 1. FE-SEM of WT samples irradiated for (A) 0, (B) 3, (C) 6 and (D) 9 min, and AL samples irradiated for (E) 0, (F) 3, (G) 6 and (H) 9 min.

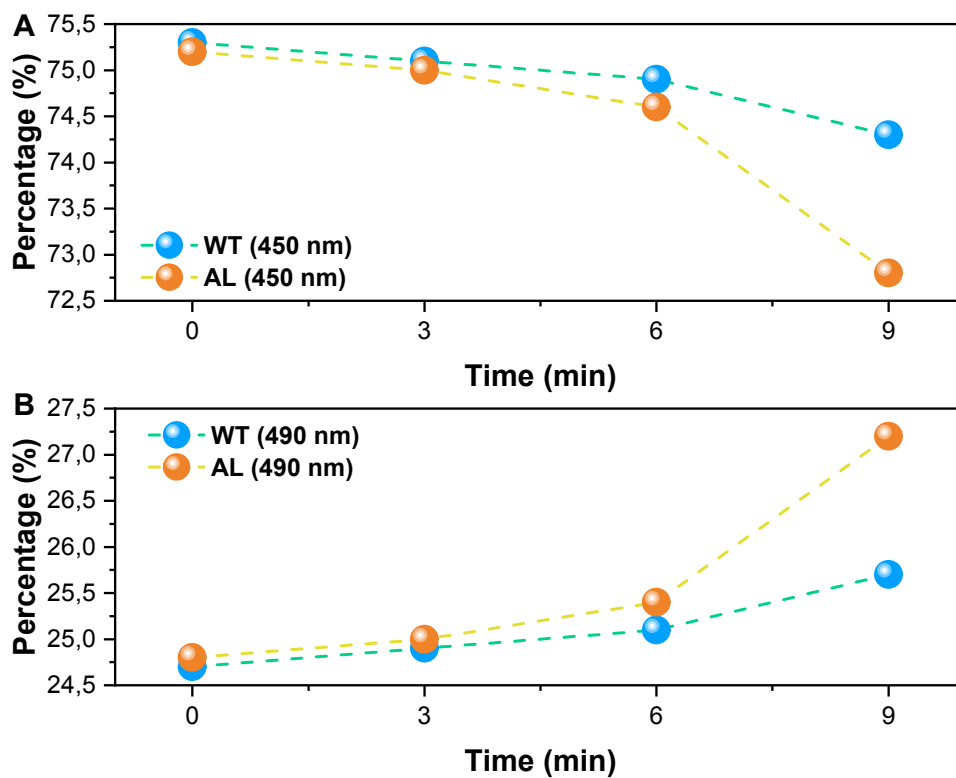


Figure 2. Percentages of PL deconvolution components for samples located at (A) 450 and (B) 490 nm as a function of EBI time.

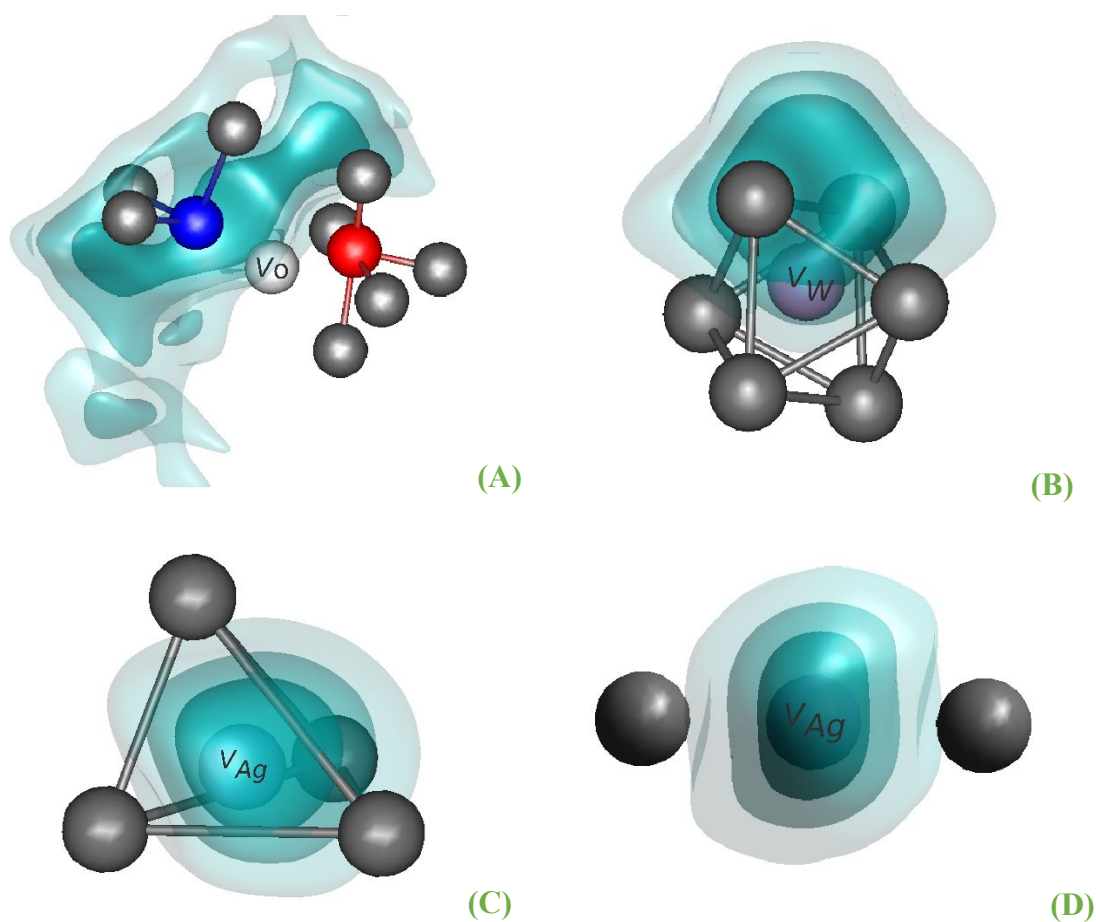


Figure 3. Positron wavefunction isodensities calculated for monovacancy states: **(A)** a V_O created between one $[WO_6]$ and one $[AgO_4]$ clusters; **(B)** a V_W created inside a $[WO_6]$ cluster; **(C)** a V_{Ag} formed inside an $[AgO_4]$ cluster; and **(D)** a V_{Ag} created within an $[AgO_2]$ cluster. The positron isodensities are represented by three surface contours, which correspond to 70%, 50% and 30% of the maximum positron density. For the sake of clarity, only the participating clusters are shown in the figures. W atoms are represented in red, Ag atoms in blue and O atoms in dark gray. Missing atoms related to the different monovacancies are labeled.

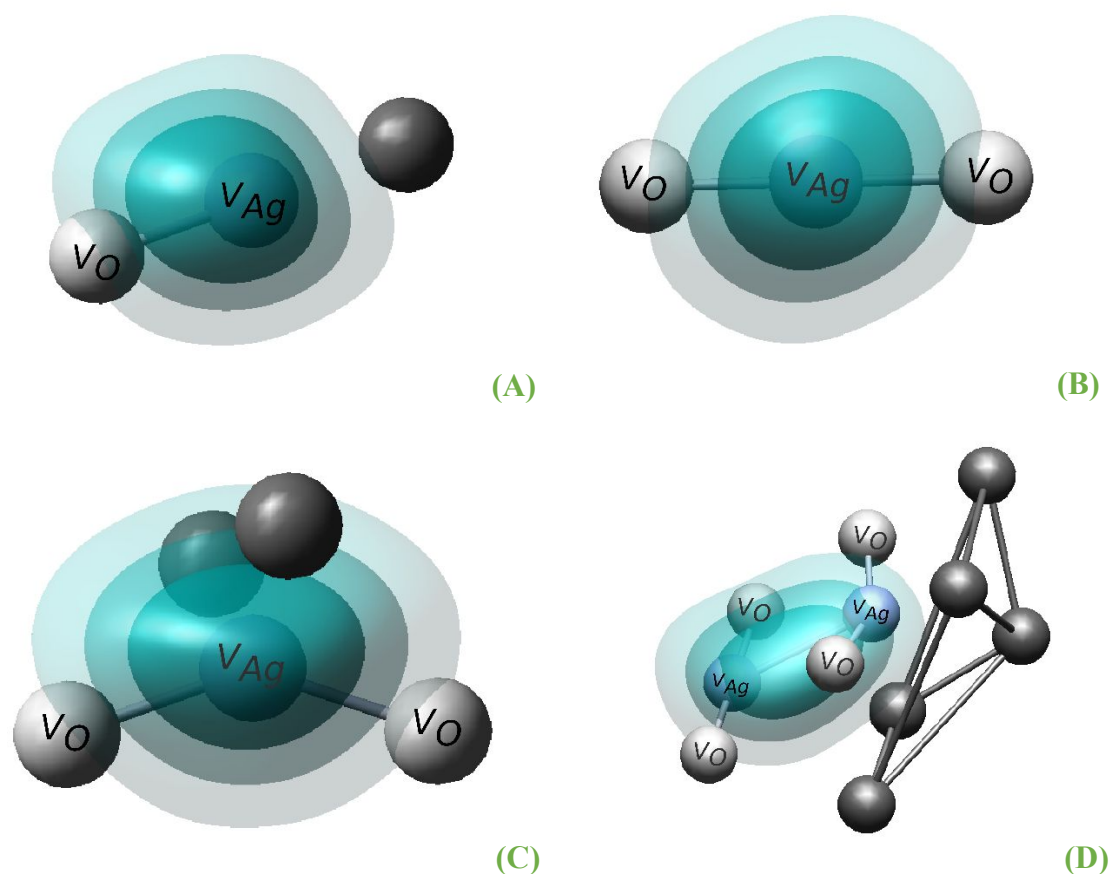


Figure 4. Positron wavefunction isodensities calculated for vacancy complexes: **(A)** a $V_{Ag} + V_O$ divacancy created inside an $[AgO_2]$ cluster; **(B)** a $V_{Ag} + 2V_O$ trivacancy corresponding to the whole missing $[AgO_2]$ cluster; **(C)** a $V_{Ag} + 2V_O$ trivacancy formed inside an $[AgO_4]$ cluster; and **(D)** a $2V_{Ag} + 4V_O$ hexavacancy created between an $[AgO_2]$ cluster and a neighboring $[AgO_7]$ cluster. The positron isodensities are represented by three surface contours, which correspond to 70%, 50% and 30% of the maximum positron density within the contour. For the sake of clarity, only the participating clusters are shown in the figures. W atoms are represented in red, Ag atoms in blue and O atoms in dark gray. Missing atoms related to the different monovacancies forming the vacancy complexes are labeled.

1
2
3
4
5
6
7
8
9
10
11
12
13
14
15
16
17
18
19
20
21
22
23
24
25
26
27
28
29
30
31
32
33
34
35
36
37
38
39
40
41
42
43
44
45
46
47
48
49
50
51
52
53
54
55
56
57
58
59
60

Table 1. Values of positron lifetimes and their associated intensities obtained from the decomposition of PALS spectra for α -Ag₂WO₄ microcrystalline WT samples irradiated and non-irradiated at different times.

<i>Irradiation time (min)</i>	τ_1 (ps)	I_1 (%)	τ_2 (ps)	I_2 (%)
0	172 ± 1	24.7 ± 0.5	274 ± 2	72.6 ± 0.5
3	156 ± 3	24.9 ± 0.5	274 ± 2	75.1 ± 0.5
6	154 ± 2	21.0 ± 0.5	271 ± 1	79.0 ± 0.5
9	141 ± 1	20.0 ± 0.5	263 ± 1	80.0 ± 0.5

Table 2. Values of positron lifetimes and their associated intensities obtained from the decomposition of PALS spectra for α -Ag₂WO₄ microcrystalline AL samples irradiated and non-irradiated at different times.

<i>Irradiation time (min)</i>	τ_1 (ps)	I_1 (%)	τ_2 (ps)	I_2 (%)
0	222.1 ± 0.6	61.4 ± 0.5	345 ± 2	38.6 ± 0.5
3	214.4 ± 0.5	50.8 ± 0.5	324 ± 2	49.2 ± 0.5
6	204.4 ± 0.5	39.0 ± 0.5	299 ± 1	61.0 ± 0.5
9	182.7 ± 0.5	24.8 ± 0.5	286 ± 1	75.2 ± 0.5

Table 3. Values of positron lifetimes, τ , and binding energy, E_b , for different positron defect states in the α - Ag_2WO_4 structure.

<i>Cluster</i>	<i>Defect state</i>	τ (ps)	E_b (eV)
<i>bulk</i>	-	172	-
<i>[WO₆], [AgO_x] (x = 2, 4, 6 and 7)</i>	V_O	173	~ 0
	V_W	178	0.1
<i>[AgO₂]</i>	V_{Ag}	230	0.6
	$V_{Ag} + V_O$	255	0.8
	$V_{Ag} + 2V_O$	275	1.0
<i>[AgO₄]</i>	V_{Ag}	225	0.6
	$V_{Ag} + V_O$	250	0.8
	$V_{Ag} + 2V_O$	265	0.9
<i>[AgO₆]</i>	V_{Ag}	204	0.4
	$V_{Ag} + V_O$	223	0.5
	$V_{Ag} + 2V_O$	239	0.7
<i>[AgO₇]</i>	V_{Ag}	227	0.6
	$V_{Ag} + V_O$	250	0.8
	$V_{Ag} + 2V_O$	264	0.9
-	$2V_{Ag} + 4V_O$	311	1.2

TOC



- 1
- 2
- 3
- 4
- 5
- 6
- 7
- 8
- 9
- 10
- 11
- 12
- 13
- 14
- 15
- 16
- 17
- 18
- 19
- 20
- 21
- 22
- 23
- 24
- 25
- 26
- 27
- 28
- 29
- 30
- 31
- 32
- 33
- 34
- 35
- 36
- 37
- 38
- 39
- 40
- 41
- 42
- 43
- 44
- 45
- 46
- 47
- 48
- 49
- 50
- 51
- 52
- 53
- 54
- 55
- 56
- 57
- 58
- 59
- 60